ACSNANO

www.acsnano.org

ARTICLE

Evidence of Josephson Coupling in a Few-Layer Black Phosphorus Planar Josephson Junction

Francesca Telesio, Matteo Carrega, Giulio Cappelli, Andrea Iorio, Alessandro Crippa, Elia Strambini, Francesco Giazotto, Manuel Serrano-Ruiz, Maurizio Peruzzini, and Stefan Heun*

Cite This: *ACS Nano* 2022, 16, 3538−3545

Read Online

ACCESS | Metrics & More | Article Recommendations | Supporting Information

ABSTRACT: **Setting up strong Josephson coupling in van der Waals materials in close proximity to superconductors offers several opportunities both to inspect fundamental physics and to develop cryogenic quantum technologies. Here we show evidence of Josephson coupling in a planar few-layer black phosphorus junction. The planar geometry allows us to probe the junction behavior by means of external gates, at different carrier concentrations. Clear signatures of Josephson coupling are demonstrated by measuring supercurrent flow through the junction at milli-Kelvin temperatures. Manifestation of a Fraunhofer pattern with a transverse magnetic field is also reported, confirming the Josephson coupling. These findings represent evidence of proximity Josephson coupling in a planar junction based on a van der Waals material beyond graphene and will expedite further studies, exploiting the peculiar properties of exfoliated black phosphorus thin flakes.**

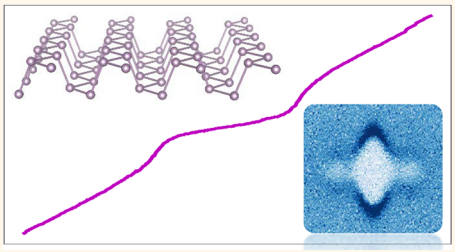

KEYWORDS: *Josephson junctions, black phosphorus, quantum devices, van der Waals materials, planar geometry*

To date, Josephson junction (JJ) devices find a wide range of applications, such as highly sensitive magnetometers,[1] infrared sensors,[2−4] single-photon detectors,[4] and superconducting quantum circuits for quantum information purposes.[5] Moreover, hybrid JJs formed with semiconductors placed in between two superconducting contacts have attracted great interest,[6−15] due to the possibility of tuning their superconducting properties by external electrostatic gates. Among all, high-quality two-dimensional electron gases (2DEGs) have been inspected in so-called planar JJs, exploiting peculiar features such as long ballistic transport and conductance quantization in combination with proximity-induced superconducting correlations.[15−22]

In the study of 2D materials, recent advances in mechanical exfoliation techniques allowed for the fabrication of devices with thickness ranging from a single 2D layer, like graphene and its van der Waals relatives, to multilayer systems with different and tunable properties.[23−33] Planar junctions based on 2D exfoliated materials constitute a very interesting and intriguing platform for several reasons. To start with, such devices offer the great opportunity to study fundamental aspects of distinct physics, such as Dirac-like relativistic behavior in combination with superconductivity,[34−37] and are a promising platform for advanced sensing and detection down to the single photon in a wide spectral range.[4] Importantly, the superconducting contacts can be placed laterally, retaining the surface of the device free, allowing for the spatially resolved investigation of correlations and transport properties, providing also the possibility to add top gates. This has triggered great experimental efforts to realize hybrid JJs with 2D flakes and led in 2007 to the fabrication and characterization of a graphene-based JJ device,[34] demonstrating a bipolar tuning of supercurrent amplitude with well-developed Josephson coupling.

Since then, a vast variety of graphene−superconductor hybrid structures have been explored (see ref 36 and references therein), with an improved quality of both the graphene samples and the transparency of the interfaces. This allowed to investigate proximity-induced superconductivity in graphene junctions from the diffusive to the ballistic regime. Interestingly, the coexistence of superconductivity and quantum Hall regime has been reported recently in this platform,[38−41] promoting graphene-based JJs as a good candidate to investigate the emergence of topological states of matter.[42,43]

Received: October 21, 2021
Accepted: January 26, 2022
Published: January 31, 2022

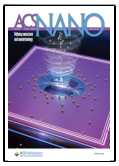

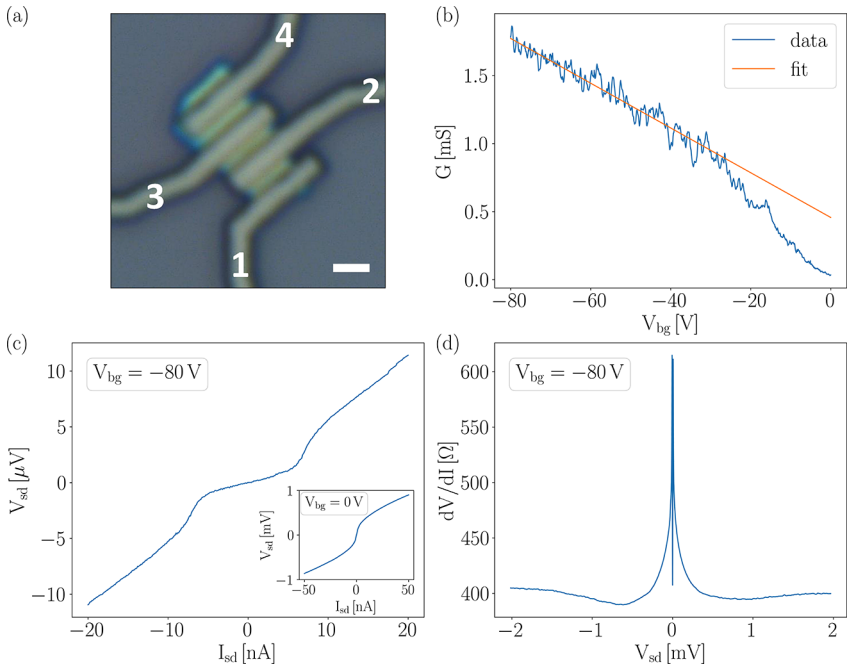

Figure 1. (a) Optical microscopy image of the device. Contact numbers are indicated in the figure. Scale bar: 1 μm. (b) Conductance G *versus* back gate voltage V_{bg} from −80 to 0 V, measured in current bias with a current of 20 nA. The straight line is a linear fit to the data from V_{bg} = −80 V to −30 V, used to calculate the hole mobility. (c) V_{sd} as a function of I_{sd} at a back gate voltage V_{bg} = −80 V. The inset shows the same for a back gate voltage of 0 V. (d) Differential resistance dV/dI of the junction in a wide range of bias values V_{sd} at V_{bg} = −80 V. The central dip is due to the supercurrent in the junction. All data were measured at B = 0 mT and T = 33 mK.

Graphene is only one example of the large family of van der Waals materials that can be exfoliated down to monolayer thickness.[26−33] However, to date, clear signatures of Josephson coupling in other van der Waals-based planar JJs have not been reported. We note that finite Josephson coupling in a vertical structure including a 5 to 10 nm thick spacing layer of black phosphorus (bP) in between Nb slabs[44,45] and in a vertical interconnect between MoS_2 and MoRe[46] has been reported recently. In these structures, the semiconducting van der Waals material is used as a thin, almost transparent barrier, and the transport in the vertical direction, across the layers, is probed. There, however, gate tuning of the proximitized system is very difficult and can be achieved only laterally, resulting in a strong anisotropic modulation of carrier density in the semiconducting material.[45] In this respect, planar junctions represent a scalable and versatile technology, where homogeneous gating can be easily obtained. In addition, planar junctions allow the investigation of the superconducting proximity effect in the extreme single layer (monolayer) limit, which is not possible in the vertical configuration.

In this work, we report on the fabrication and characterization of planar JJ devices based on few-layer black phosphorus. bP is a layered semiconducting material, whose peculiar properties mainly stem from the anisotropic shape of its band structure, which affects both its electronic and optical properties.[30−33,47−50] Theoretical studies for superconducting JJs with monolayer bP have been put forward, with intriguing features that may emerge in ballistic samples in combination with ferromagnetic elements.[51−53]

Here, we perform transport measurements on bP planar JJs with Nb contacts at cryogenic temperatures down to T = 33 mK, demonstrating supercurrent flow and clear evidence of Josephson coupling.

RESULTS AND DISCUSSION

Exfoliated bP flakes were deposited on B-doped Si substrates. A geometry with four parallel contacts was designed to allow for the characterization of several JJs on a single BP flake. The devices were realized by electron beam lithography, with a procedure described in detail in the Methods section. Air exposure was minimized throughout the fabrication process, and a combined oxygen−argon plasma process was optimized to enhance the interface quality. Moreover, an Ar etching, described in detail in the Methods section, was performed *in situ*, to remove any residual oxide under the contacts. Superconducting Ti/Nb contacts of 10/60 nm thickness were deposited by a sputtering technique. The critical temperature T_c of the Ti/Nb electrodes was measured to be 8.3 ± 0.2 K, which corresponds to a bulk superconducting gap of the electrodes of $\Delta_S = 1.76 k_B T_c$ = 1.26 ± 0.03 meV, in line with the expected value for bulk Nb.[21,22,54]

The devices shown in Figure 1(a) have a length of the individual JJs of $L \approx$ 500 nm, while their widths W range from 1.6 μm (between contacts 1−2) to 2.0 μm (between contacts 2−3 and 3−4), due to a slight trapezoidal shape of the bP flake. We estimate the uncertainty in these numbers to be ±25 nm. The flake thickness of the few-layer bP, inferred from the optical microscopy image, is about 10 nm. In the following, we will present results obtained between contacts 2 and 3 (with contacts 1 and 4 floating). We underline that we have obtained consistent results from device 1−2 (shown in Figure S5 in the Supporting Information).

Black phosphorus is an intrinsically p-type semiconductor.[47−49] For a back gate voltage V_{bg} = −80 V, the bP is deep in the p-type branch. Sweeping the back gate toward zero voltage, the Fermi level of the semiconductor is shifted into the band gap, which results in a strong increase in resistance or, equivalently, a strong decrease in conductance. This is shown

https://doi.org/10.1021/acsnano.1c09315
ACS Nano 2022, 16, 3538−3545

in the back gate sweep in Figure 1(b), which was measured in current bias with a current amplitude of 20 nA. A further increase of the back gate voltage to +80 V drives the device into the n-type regime, as shown in the Supporting Information. From the back gate sweep, a field effect mobility $\mu = 360\ \mathrm{cm}^2/(\mathrm{V\ s})$ is obtained from a linear fit of G *versus* V_{bg} in the range −30 V to −80 V.

Figure 1(c) shows the $V-I$ characteristics of the device measured in a current bias configuration at a back gate voltage of −80 V. A clear and pronounced Josephson supercurrent with an amplitude of 5 nA is observed. Once the bias current exceeds this critical value, the device switches from the superconducting to the normal state, with a resistance of R_N = 560 Ω. As can be seen in Figure 1(c), the differential resistance around $I_{sd} = 0$ is not strictly zero but $R_0 \approx 200\ \Omega$. This is due to the effect of thermal fluctuations in the junction and can be understood in the framework of the theory by Ambegaokar and Halperin.[55,56] In fact, the McCumber parameter β_c of the junction is $\beta_c = \omega_J \tau_{RC}$, with $\omega_J = 2eV_c/\hbar$ the characteristic Josephson frequency ($\hbar$ is the reduced Planck constant, $V_c = I_c R_N$, with I_c the critical current) and $\tau_{RC} = R_N C$ the decay time within the RCSJ model.[56−58] Approximating the junction capacitance C with a parallel plate capacitor model, we obtain $\beta_c = 1.2 \times 10^{-5} \ll 1$ (for details, see the Supporting Information). Thus, the junction is in the overdamped regime, and the nonvanishing junction voltage even in the limit $I_{sd} \to 0$ can be attributed to a phase-slip resistance contribution. Consistent with this interpretation, the measured $V-I$ curves do not show any hysteresis; that is, switching and retrapping current, I_{sw} and I_{rt}, respectively, are equal.

Finally, we inspect the behavior of the junction at elevated bias, to look for any subharmonic gap features. Figure 1(d) shows the differential resistance, measured at $V_{bg} = -80$ V. The supercurrent branch is resolved as the central dip, due to the reduced resistance in the $V-I$ curve at the origin. The differential resistance curve shown in Figure 1(d) does not show any evidence for multiple Andreev reflections (MARs), but instead a clear Schottky behavior, with an increased resistance at small bias. This indicates that at small bias the transparency of the S/N interface is not ideal, and the Josephson junction is better described as a SINIS structure, *i.e.*, a superconductor−insulator−normal−insulator−superconductor hybrid system. From Figure 1(d), we can estimate the resistance R_i of each S−N interface from the difference in differential resistance at low bias ($R_N = 560\ \Omega = R_{bP} + 2R_i$) and at high bias ($R_{bP} = 400\ \Omega$, see Figure 1(d)). This gives $R_i = 80\ \Omega$. The hypothesis of opaque S/N interfaces is further supported by the lack of excess current as described in the Supporting Information.

The Schottky barrier is further increased at lower carrier concentrations, as shown in the inset to Figure 1(c), which shows that at $V_{bg} = 0$ V, in contrast to the observation at $V_{bg} = -80$ V, no supercurrent is observed, and the $V-I$ curve rather shows a Schottky-like behavior. In line with the above discussion, this confirms the presence of a Schottky barrier at the interface between bP and the superconductor, preventing a Josephson coupling at $V_{bg} = 0$ V. Also in the n-type regime, as shown in the Supporting Information, the quality of the contacts does not improve, consistent with previous observations,[59] and the metal−semiconductor contacts are still dominated by the Schottky barrier, which prevents observation of a bipolar signal in supercurrent amplitude. Thus, in the following we will focus on the accumulation region.

From the data shown in Figure 1, important information on the transport in the junction can be extracted. The sheet resistance R_s of bP at $V_{bg} = -80$ V is $R_s = (W/L)R_{bP} = 1.6\ \mathrm{k\Omega}/\square$. Within a two-dimensional Drude model we obtain a carrier concentration at $V_{bg} = -80$ V of $n = 1.1 \times 10^{13}\ \mathrm{cm}^{-2}$. Using $l_e = \hbar k_F \mu/e$ and the Fermi wave vector $k_F = \sqrt{2\pi n}$,[60] we estimate the elastic mean free path to be $l_e = 20$ nm. This places the junction in the diffusive regime, since the mean free path is much smaller than the length of the junction, $l_e \ll L$. The coherence length of the N region (bP) is[61] $\xi_N = \sqrt{\hbar D/(2\pi k_B T)} = 290$ nm at 33 mK, which reduces to 100 nm at 300 mK. Here, $D = v_F l_e/2 = \hbar^2 \pi/(e^2 m^* R_s)$ is the diffusion coefficient in the bP and $m^* = 0.41 m_0$ the average in-plane effective mass of holes in bP.[50,62] Therefore, L is greater than ξ_N. This indicates that the device operates in the long-junction regime.[22,54,63]

The natural energy scale for the proximity effect is the Thouless energy[64−66] $E_{Th} = \hbar D/L^2$; here $E_{Th} = 6.0\ \mu$eV. Thus, $\Delta_S \gg E_{Th}$. The thermal energy $k_B T$ is slightly smaller than E_{Th} (here $k_B T = 2.8\ \mu$eV) and also smaller than the Josephson energy[66] $E_J = \hbar I_c(T)/2e$ (here $E_J = 10.3\ \mu$eV), however, sufficiently large that thermal fluctuations would be relevant, supporting an interpretation of the data in terms of the Ambegaokar−Halperin picture.[55,56]

The supercurrent in the junction can be controlled by an external back gate. This is shown in Figure 2(a), which shows the differential resistance $\mathrm{d}V/\mathrm{d}I$ of the junction as a function of bias current I_{sd} and back gate voltage V_{bg}. Reducing the back gate voltage from −80 to 0 V, the switching current is reduced from 5 nA to zero. This reduction in supercurrent is accompanied by an increase in the resistance of the normal branch (evaluated at $I_{sd} = 20$ nA). Figure 2(b) shows, on the left axis, the switching current as a function of back gate voltage, while the right axis shows the corresponding energy scale, obtained *via* $E_J = \hbar I_{sw}/2e$. Figure 2(b) shows that a reduction of the back gate voltage reduces the Thouless energy E_{Th} (*via* an increase in the sheet resistance). At about $V_{bg} = -40$ V, the Josephson energy E_J, which is proportional to the critical current, becomes smaller than the thermal energy $k_B T$. Beyond this point I_{sw} displays strong thermal fluctuations, until a complete suppression is observed at $V_{bg} = -25$ V, a back gate voltage at which also the Thouless energy becomes smaller than the thermal energy $k_B T$. Also at about $V_{bg} = -25$ V, the resistance at zero current R_0 becomes larger than the resistance in the normal branch, underlining the quenching of the Josephson coupling due to the increased Schottky barrier, as also shown in the $V-I$ curves in Figure 1(c).

The monotonic decay of $I_{sw}(V_{bg})$ is well described in the framework of diffusive Josephson junctions with opaque S/N interfaces.[12,67,68] The details of the theoretical model are described in the Methods section. As shown in Figure 2(b), the model can accurately describe the monotonic decay of $I_{sw}(V_{bg})$, adding further evidence for the presence of a Schottky barrier at the interface between bP and the superconductor.

It is well known that an increase in temperature suppresses proximity-induced superconductivity. Figure 3(a) reports the temperature dependence of the differential resistance. The figure clearly shows that at ∼500 mK supercurrent is suppressed, and an ohmic behavior of the junction is observed. Two effects lead to this evolution: first, the value of the

https://doi.org/10.1021/acsnano.1c09315
ACS Nano 2022, 16, 3538−3545

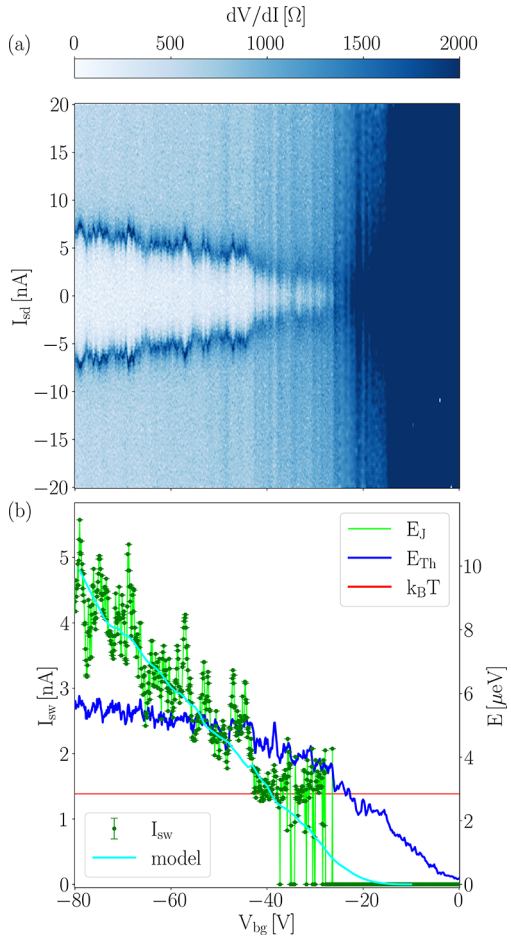

Figure 2. (a) Differential resistance dV/dI of the junction as a function of bias current I_{sd} and back gate voltage V_{bg}. (b) Left axis: switching current I_{sw} evaluated from (a), and right axis: the two relevant energy scales, Josephson energy E_J and Thouless energy E_{Th}, as a function of back gate voltage V_{bg}, compared to the thermal energy k_BT. The Josephson energy is evaluated from the switching current $E_J = \hbar I_{sw}/2e$, while $E_{Th}(V_{bg}) = \hbar D/L^2$ is obtained from the transconductance of the junction (see the Methods section for more details). The transconductance has also been used in a theoretical model for the critical current I_c including a sizable interface resistance and shown in (b) superimposed on the experimental data. B = 0 mT, T = 33 mK.

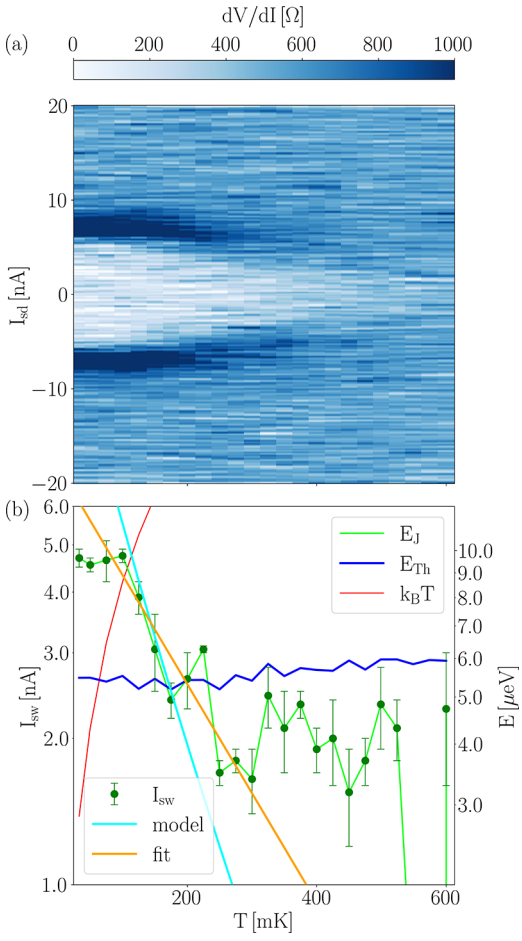

Figure 3. (a) Differential resistance dV/dI of the junction as a function of bias current I_{sd} and temperature T. (b) Left axis: switching current I_{sw} on a logarithmic scale as a function of temperature T. Error bars are the standard deviation of the measured data. The fitted line indicates an exponential decay of the switching current with temperature, which is also captured by the theoretical model. Right axis: the corresponding energy scale. E_{Th} is obtained *via* R_s, which is calculated from the measured R_N using eq 2 (see Methods for more details). B = 0 mT, V_{bg} = −80 V.

switching current is reduced by temperature. At the same time, the slope R_0 of the V−I curves at I_{sd} = 0 increases due to thermally activated phase slips. An Arrhenius plot of $\ln(R_0)$ *vs* $1/T$ (Figure S6 of the Supporting Information) shows a linear trend between 200 and 600 mK, with slope −256.0 mK. According to Halperin *et al.*,[69] $R_0 \propto e^{-2E_J/k_BT}$. From this, E_J = 11 μeV is obtained, in good agreement with the value of E_J obtained at base temperature (33 mK).

Figure 3(b) shows, on the left y-axis, the switching current as a function of temperature on a logarithmic scale. The right axis shows the corresponding energy scale. The graph shows that the Thouless energy E_{Th} is approximately constant, since the normal resistance does not change significantly in this temperature range. At low temperatures, the supercurrent appears to be approximately constant until k_BT becomes larger than E_J, possibly due to a saturation of electron temperature below 100 mK. Above that point, a linearly decreasing trend in switching current and thus in Josephson energy is observed (on a log-scale), compatible with an exponential decrease with temperature. However, when the Josephson energy becomes approximately equal to the Thouless energy, a deviation from this exponential decrease is observed, with $E_J \approx E_{Th}$, until finally at $T \approx$ 500 mK the switching current drops to zero. An exponential decrease in switching current is typical of ballistic long junctions,[22,63] but a quasi-exponential temperature dependence of the critical current is also expected for a diffusive system in the long junction regime, as shown by Courtois and Schön.[66,70,71] An analysis of the measured switching current with the function $I_{sw} = I_0 \exp(-T/T^*)$ yields as best fit parameters I_0 = 7.3 nA and T^* = 194 mK. The fit is also indicated in Figure 3(b). According to Wilhelm *et al.*,[71] $k_BT^* = 12E^*/\pi$, with $E^* = E_{Th}(1 + 0.7R_i/R_{bP})$,[68] and thus from T^* we get a value of the Thouless energy of 5.0 μeV, in excellent agreement with the value obtained from the data shown in Figure 1. Overall, this analysis underlines the importance of the Thouless energy as the relevant energy scale, since here $E_{Th} \ll \Delta_S$.

Also in this case, the temperature dependence of I_{sw} can be well represented by the theoretical model of a diffusive

https://doi.org/10.1021/acsnano.1c09315
ACS Nano 2022, 16, 3538−3545

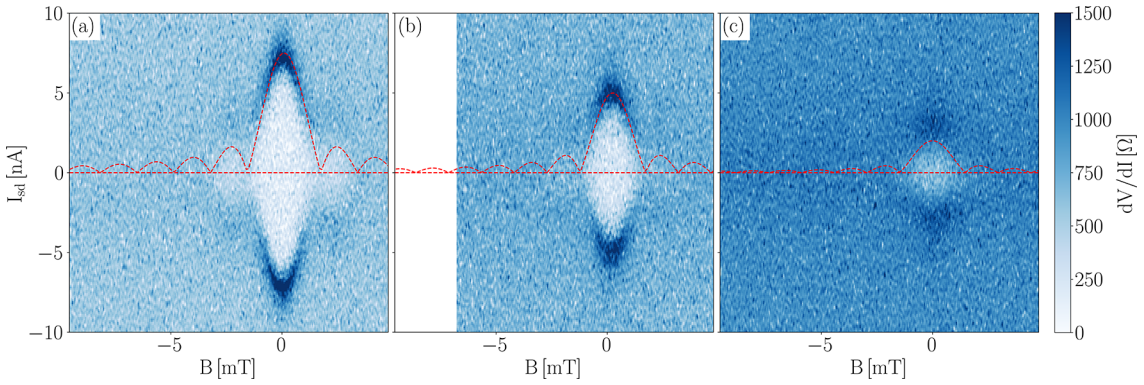

Figure 4. Differential resistance dV/dI of the junction as a function of bias current I_{sd} and magnetic field B. (a) V_{bg} = −80 V, (b) V_{bg} = −60 V, (c) V_{bg} = −40 V. A fit to the standard Fraunhofer formula is plotted as a dashed red line in each panel. T = 33 mK.

mesoscopic Josephson weak link with opaque interfaces (cyan curve in Figure 3(b)). Notably, the same model with clean interfaces yields an I_c one order of magnitude higher, demonstrating the importance of the opaque interfaces in the estimation of I_c.

A clear signature of a well-established Josephson coupling in a JJ device is the presence of a Fraunhofer pattern, when a magnetic field perpendicular to the junction is applied. Figure 4 shows the differential resistance dV/dI of the junction *versus* bias current I_{sd} and perpendicular magnetic field B, measured for three different back gate voltages. The presence of a Fraunhofer pattern centered at B = 0 mT is clearly visible, consistent with a strong Josephson coupling at zero magnetic field. Applying a small magnetic field, the supercurrent is gradually reduced to zero at |B| = 1.65 mT; then it reappears, and at |B| > 3.3 mT it completely disappears. This behavior is characteristic of a Fraunhofer pattern with a central lobe and two side lobes, and the suppression of supercurrent by a small magnetic field clearly points at the proximity effect as the origin of the observed behavior of the V−I curves around zero bias. The Fraunhofer patterns measured at different back gate voltages consistently follow the general trend shown in Figure 2: the supercurrent is reduced by a lower negative voltage on the back gate, while the normal resistance is increased. However, the periodicity of the Fraunhofer pattern remains the same as for V_{bg} = −80 V, adding further support to the interpretation of these data in terms of induced superconducting proximity within the junction.

These data were analyzed with the well-known conventional Fraunhofer formula $I_c(B) = I_c(0)|\sin(\pi\Phi/\Phi_0)/(\pi\Phi/\Phi_0)|$, with $I_c(0)$ the critical current at zero magnetic field, Φ the magnetic flux, and $\Phi_0 = h/2e$ the superconducting flux quantum.[72,73] The corresponding Fraunhofer patterns are included in Figure 4 as dashed red lines. From the periodicity of the Fraunhofer pattern, we extract a characteristic area of 1.35 ± 0.07 μm^2, in good agreement with the effective geometrical area of the junction[74] $A = W(L + 2\lambda_L) = 1.16 \pm 0.06$ μm^2, with λ_L = 39 ± 5 nm the London penetration depth of Nb.[75] The slight difference between the two values can be explained by a magnetic field focusing due to the Meissner effect.[22,76,77]

CONCLUSIONS

In summary, we have presented transport measurements on bP planar JJs with Ti/Nb contacts performed at cryogenic temperatures down to T = 33 mK, demonstrating a sizable supercurrent up to 5 nA and unequivocal evidence of Josephson coupling. The supercurrent can be controlled by a back gate. Application of a small perpendicular magnetic field leads to the formation of a well-developed Fraunhofer pattern. Supercurrent signal disappears above a temperature of 500 mK. All these observations are clear manifestations of proximity-induced superconductivity in the bP planar junction and place bP in the spotlight as a valid 2D van der Waals material for applications in quantum technology. We anticipate that optimization of the ohmic contacts to the bP will improve device performance and eventually allow the observation of ambipolar supercurrent in such devices. Further progress in device fabrication, *e.g.*, by encapsulation of the bP flakes in hexagonal boron nitride, will allow the realization of ballistic junctions, in which the crystalline anisotropy of bP might be employed for innovative devices and quantum sensors. Among all, bP devices are exploited as widely tunable infrared photodetectors,[78−80] and optimized bP-based planar Josephson junctions are thus a promising platform for infrared single-photon detectors.[4,81]

METHODS

Device Fabrication. BP crystals were fabricated following a well-established procedure.[82] For details, see the Supporting Information. There we also show a Raman spectrum of the flake used in this work. The high reactivity of exfoliated bP represents the major challenge for the realization of high-quality devices, including JJ-like devices, where the quality of the interfaces represents one of the main bottlenecks. To address this issue, bP exfoliation was carried out in a glovebag under a nitrogen atmosphere. After the transfer of the flakes onto the Si wafer substrate, the samples were immediately coated with a layer of protective polymer (poly(methyl methacrylate), PMMA), which is also the lithographic resist. The geometry of the device was defined by electron beam lithography (EBL) using a Zeiss Ultraplus SEM equipped with Raith Elphy Multibeam software. After development of the resist, a combined and optimized cleaning procedure was applied to the sample.[83] First, a mild oxygen plasma of 10 W for 1 min with 40 sccm of oxygen was performed to efficiently remove all the resist residuals. Then the sample was transferred to the vacuum chamber for the metal sputtering, and an *in situ* cleaning with Ar plasma was performed at 50 mTorr with 4 W power for 30 min. The etching conditions were tuned to have a gentle etching and a better control of the process. The etching time was calibrated to minimize the contact resistance. This last cleaning step was performed after the presputtering of the two metallic targets for metal deposition, during which the sample was preserved from contamination thanks to a closed shutter and a rotating carousel that allowed moving the sample away from the plasma source. Then 10 nm of Ti and 60 nm of Nb were deposited. The Ti layer was found to decrease the contact resistance and to allow for a better growth of the Nb overlayer. In fact,

https://doi.org/10.1021/acsnano.1c09315
ACS Nano 2022, 16, 3538−3545

an average increase of the critical temperature of the devices with a Ti layer was observed, compared to devices with an Al/Nb bilayer or with Nb grown directly onto the bP.[83] After the sputtering process, the sample underwent a fast lift-off in acetone at 55 °C. Then it was immediately coated with a bilayer of methyl methacrylate methacrylic acid copolymer and PMMA, to guarantee protection from oxidation. This protection layer is more than 500 nm thick; therefore holes for the bonding pads have been opened in a second EBL step.

Transport Measurements. The low-temperature transport data were measured in a filtered closed-cycle dilution refrigerator from Leiden Cryogenics with a base temperature of $T = 33$ mK. $V-I$ curves were measured in DC current biasing, using a Yokogawa DC source on a 10 MΩ bias resistor. The voltage drop across the junction was measured in four-probe configuration with a DL Instruments voltage preamplifier (gain 10^4) and an Agilent multimeter, while the current was measured with a DL Instruments current preamplifier (gain 10^7) and another Agilent multimeter. The back gate was biased with a Keithley DC source. We have verified that the loss current from gate to sample was below the detection limit of the source meter. The differential resistance measurements shown in Figure 1(d) were obtained with a DC + AC signal, using a standard AC lock-in technique with current excitation in the range 5 to 10 nA.

Model. The observed behavior of the critical current I_c of the junction can be modeled by solving the associated quasi-classical Usadel equation.[84] To properly reproduce the experimental data, a sizable S/N interface resistance (R_i) has been introduced, considering diffusive Josephson junctions with opaque S/N interfaces. In this case, the critical current can be obtained by[12,67,68]

$$I_c = \frac{2\pi k_B T}{eR_{bP}} \sum_{n=0}^{\infty} \frac{(k_{\omega_n} L)\Delta^2}{(\omega_n^2 + \Delta^2)[\alpha \sinh(k_{\omega_n} L) + \beta \cosh(k_{\omega_n} L)]} \quad (1)$$

where the sum over Matsubara frequencies $\omega_n = (2n + 1)\pi k_B T$ is carried out numerically. Here, k_B is the Boltzmann constant, $k_{\omega_n} = \sqrt{2\omega_n/(\hbar D)}$, $R_{bP} = R_N - 2R_i$ is the resistance of the junction excluding the interfaces, $\alpha = 1 + (rk_{\omega_n} L)^2$, $\beta = 2rk_{\omega_n} L$, and $r = R_i/R_{bP}$. Using eq 1 it is possible to calculate the temperature dependence of the critical current (Figure 3(b)). The best fit to the experimental data was obtained with $L = 650$ nm and $T = 110$ mK. The same model has been used to simulate the evolution of the critical current as a function of the gate voltage (Figure 2(b)). The gate affects the resistance of the junction and as a consequence the diffusion constant D. The variation of r with back gate voltage was approximated by a linear function:

$$r = 3.86 \times 10^{-3}\ V^{-1} \cdot V_{bg} + 4.83 \times 10^{-1} \quad (2)$$

which was the best fit to $r(V_{bg})$ data extracted from a series of $V-I$ curves measured in a wide bias range at different back gate voltages. This allows calculating R_s from R_N in measurements for which the bias range was not wide enough to determine R_s directly. Finally, this allows the calculation of the diffusion constant D from R_N.

ASSOCIATED CONTENT

Supporting Information

The Supporting Information is available free of charge at https://pubs.acs.org/doi/10.1021/acsnano.1c09315.

Additional information on device fabrication; Raman spectroscopy data (Figure S1); calculation of the McCumber parameter β_c; additional transport characterization; additional back gate sweeps (Figure S2), additional $V-I$ curves (Figures S3, S4); data from device 1−2 (Figure S5); Arrhenius plot (Figure S6) (PDF)

AUTHOR INFORMATION

Corresponding Author

Stefan Heun − *NEST, Istituto Nanoscienze-CNR and Scuola Normale Superiore, 56127 Pisa, Italy;* orcid.org/0000-0003-1989-5679; Email: stefan.heun@nano.cnr.it

Authors

Francesca Telesio − *NEST, Istituto Nanoscienze-CNR and Scuola Normale Superiore, 56127 Pisa, Italy;* orcid.org/0000-0003-3834-3685

Matteo Carrega − *CNR-SPIN, 16146 Genova, Italy*

Giulio Cappelli − *NEST, Istituto Nanoscienze-CNR and Scuola Normale Superiore, 56127 Pisa, Italy*

Andrea Iorio − *NEST, Istituto Nanoscienze-CNR and Scuola Normale Superiore, 56127 Pisa, Italy*

Alessandro Crippa − *NEST, Istituto Nanoscienze-CNR and Scuola Normale Superiore, 56127 Pisa, Italy*

Elia Strambini − *NEST, Istituto Nanoscienze-CNR and Scuola Normale Superiore, 56127 Pisa, Italy;* orcid.org/0000-0003-1135-2004

Francesco Giazotto − *NEST, Istituto Nanoscienze-CNR and Scuola Normale Superiore, 56127 Pisa, Italy*

Manuel Serrano-Ruiz − *CNR-ICCOM, 50019 Sesto Fiorentino, Italy;* orcid.org/0000-0002-6372-3586

Maurizio Peruzzini − *CNR-ICCOM, 50019 Sesto Fiorentino, Italy;* orcid.org/0000-0002-2708-3964

Complete contact information is available at: https://pubs.acs.org/10.1021/acsnano.1c09315

Notes

The authors declare no competing financial interest.

ACKNOWLEDGMENTS

The authors thank Stefano Roddaro for granting access to a 2.4 K cryostat in the initial phase of this research, Filippo Fabbri for measuring the Raman spectrum, and Sebastian Bergeret for useful discussions. We acknowledge the European Research Council for funding the project PHOSFUN (Grant Agreement No. 670173) through an ERC Advanced Grant to M.P. E.S. and F.G. acknowledge the European Research Council under Grant Agreement No. 899315 (TERASEC) and the EU's Horizon 2020 research and innovation program under Grant Agreement No. 964398 (SUPERGATE) and No. 800923 (SUPERTED) for partial financial support.

REFERENCES

(1) Krey, S.; Brügmann, O.; Schilling, M. Highly Sensitive Magnetometers Based on $YBa_2Cu_3O_7$ Josephson Junction Arrays. *Appl. Phys. Lett.* **1999**, *74*, 293−295.

(2) Grimes, C. C.; Richards, P. L.; Shapiro, S. Josephson-Effect Far-Infrared Detector. *J. Appl. Phys.* **1968**, *39*, 3905−3912.

(3) Osterman, D. P.; Marr, P.; Dang, H.; Yao, C.-T.; Radparvar, M. Superconducting Infrared Detector Arrays with Integrated Processing Circuitry. *IEEE Trans. Magn.* **1991**, *27*, 2681−2684.

(4) Walsh, E. D.; Jung, W.; Lee, G.-H.; Efetov, D. K.; Wu, B.-I.; Huang, K.-F.; Ohki, T. A.; Taniguchi, T.; Watanabe, K.; Kim, P.; Englund, D.; Fong, K. C. Josephson Junction Infrared Single-Photon Detector. *Science* **2021**, *372*, 409−412.

(5) Kockum, A. F.; Nori, F. In *Fundamentals and Frontiers of the Josephson Effect*; Tafuri, F., Ed.; Springer International Publishing: Cham, 2019; pp 703−741.

(6) Beenakker, C. W. J.; van Houten, H. In *Semiconductor Heterostructures and Nanostructures*; Ehrenreich, H., Turnbull, D., Eds.; Solid State Physics; Academic Press, 1991; Vol. *44*; pp 1−228.

(7) Marsh, A. M.; Williams, D. A.; Ahmed, H. Supercurrent Transport through a High-Mobility Two-Dimensional Electron Gas. *Phys. Rev. B* **1994**, *50*, 8118−8121.
(8) Heida, J. P.; van Wees, B. J.; Klapwijk, T. M.; Borghs, G. Nonlocal Supercurrent in Mesoscopic Josephson Junctions. *Phys. Rev. B* **1998**, *57*, R5618−R5621.
(9) Schäpers, T. *Superconductor/Semiconductor Junctions*; Springer-Verlag Berlin Heidelberg, 2001.
(10) Doh, Y.-J.; van Dam, J. A.; Roest, A. L.; Bakkers, E. P. A. M.; Kouwenhoven, L. P.; De Franceschi, S. Tunable Supercurrent through Semiconductor Nanowires. *Science* **2005**, *309*, 272−275.
(11) Larsen, T. W.; Petersson, K. D.; Kuemmeth, F.; Jespersen, T. S.; Krogstrup, P.; Nygård, J.; Marcus, C. M. Semiconductor-Nanowire-Based Superconducting Qubit. *Phys. Rev. Lett.* **2015**, *115*, 127001.
(12) Tiira, J.; Strambini, E.; Amado, M.; Roddaro, S.; San-Jose, P.; Aguado, R.; Bergeret, F. S.; Ercolani, D.; Sorba, L.; Giazotto, F. Magnetically-Driven Colossal Supercurrent Enhancement in InAs Nanowire Josephson Junctions. *Nat. Commun.* **2017**, *8*, 14984.
(13) Strambini, E.; Iorio, A.; Durante, O.; Citro, R.; Sanz-Fernández, C.; Guarcello, C.; Tokatly, I. V.; Braggio, A.; Rocci, M.; Ligato, N.; Zannier, V.; Sorba, L.; Bergeret, F. S.; Giazotto, F. A Josephson Phase Battery. *Nat. Nanotechnology* **2020**, *15*, 656−660.
(14) Aggarwal, K.; Hofmann, A.; Jirovec, D.; Prieto, I.; Sammak, A.; Botifoll, M.; Martí-Sánchez, S.; Veldhorst, M.; Arbiol, J.; Scappucci, G.; Danon, J.; Katsaros, G. Enhancement of Proximity-Induced Superconductivity in a Planar Ge Hole Gas. *Phys. Rev. Research* **2021**, *3*, L022005.
(15) Moehle, C. M.; Ke, C. T.; Wang, Q.; Thomas, C.; Xiao, D.; Karwal, S.; Lodari, M.; van de Kerkhof, V.; Termaat, R.; Gardner, G. C.; Scappucci, G.; Manfra, M. J.; Goswami, S. InSbAs Two-Dimensional Electron Gases As a Platform for Topological Superconductivity. *Nano Lett.* **2021**, *21*, 9990−9996.
(16) Chrestin, A.; Matsuyama, T.; Merkt, U. Critical Currents and Supercurrent Oscillations in Josephson Field-Effect Transistors. *Phys. Rev. B* **1994**, *49*, 498−504.
(17) Mohammadkhani, G.; Zareyan, M.; Blanter, Y. M. Magnetic Interference Pattern in Planar SNS Josephson Junctions. *Phys. Rev. B* **2008**, *77*, 014520.
(18) Amado, M.; Fornieri, A.; Carillo, F.; Biasiol, G.; Sorba, L.; Pellegrini, V.; Giazotto, F. Electrostatic Tailoring of Magnetic Interference in Quantum Point Contact Ballistic Josephson Junctions. *Phys. Rev. B* **2013**, *87*, 134506.
(19) Shabani, J.; Kjaergaard, M.; Suominen, H. J.; Kim, Y.; Nichele, F.; Pakrouski, K.; Stankevic, T.; Lutchyn, R. M.; Krogstrup, P.; Feidenhans'l, R.; Kraemer, S.; Nayak, C.; Troyer, M.; Marcus, C. M.; Palmstrøm, C. J. Two-Dimensional Epitaxial Superconductor-Semiconductor Heterostructures: A Platform for Topological Superconducting Networks. *Phys. Rev. B* **2016**, *93*, 155402.
(20) Fornieri, A.; et al. Evidence of Topological Superconductivity in Planar Josephson Junctions. *Nature* **2019**, *569*, 89.
(21) Guiducci, S.; Carrega, M.; Biasiol, G.; Sorba, L.; Beltram, F.; Heun, S. Toward Quantum Hall Effect in a Josephson Junction. *Phys. Status Solidi RRL* **2019**, *13*, 1800222.
(22) Guiducci, S.; Carrega, M.; Taddei, F.; Biasiol, G.; Courtois, H.; Beltram, F.; Heun, S. Full Electrostatic Control of Quantum Interference in an Extended Trenched Josephson Junction. *Phys. Rev. B* **2019**, *99*, 235419.
(23) Geim, A. K.; Novoselov, K. S. The Rise of Graphene. *Nat. Mater.* **2007**, *6*, 183−191.
(24) Castro Neto, A. H.; Guinea, F.; Peres, N. M. R.; Novoselov, K. S.; Geim, A. K. The Electronic Properties of Graphene. *Rev. Mod. Phys.* **2009**, *81*, 109−162.
(25) Novoselov, K. S.; Fal'ko, V. I.; Colombo, L.; Gellert, P. R.; Schwab, M. G.; Kim, K. A Roadmap for Graphene. *Nature* **2012**, *490*, 192−200.
(26) Geim, A. K.; Grigorieva, I. V. Van der Waals Heterostructures. *Nature* **2013**, *499*, 419−425.
(27) Huang, M.; Li, S.; Zhang, Z.; Xiong, X.; Li, X.; Wu, Y. Multifunctional High-Performance van der Waals Heterostructures. *Nat. Nanotechnology* **2017**, *12*, 1148−1154.
(28) Jariwala, D.; Marks, T. J.; Hersam, M. C. Mixed-Dimensional van der Waals Heterostructures. *Nat. Mater.* **2017**, *16*, 170−181.
(29) Liu, Y.; Huang, Y.; Duan, X. Van der Waals Integration before and beyond Two-Dimensional Materials. *Nature* **2019**, *567*, 323−333.
(30) Liu, H.; Neal, A. T.; Zhu, Z.; Luo, Z.; Xu, X.; Tománek, D.; Ye, P. D. Phosphorene: An Unexplored 2D Semiconductor with a High Hole Mobility. *ACS Nano* **2014**, *8*, 4033−4041.
(31) Ling, X.; Wang, H.; Huang, S.; Xia, F.; Dresselhaus, M. S. The Renaissance of Black Phosphorus. *Proc. Natl. Acad. Sci. U. S. A.* **2015**, *112*, 4523−4530.
(32) Castellanos-Gomez, A. Black Phosphorus: Narrow Gap, Wide Applications. *J. Phys. Chem. Lett.* **2015**, *6*, 4280−4291.
(33) Peruzzini, M.; et al. A Perspective on Recent Advances in Phosphorene Functionalization and Its Applications in Devices. *Eur. J. Inorg. Chem.* **2019**, *2019*, 1476−1494.
(34) Heersche, H. B.; Jarillo-Herrero, P.; Oostinga, J. B.; Vandersypen, L. M. K.; Morpurgo, A. F. Bipolar Supercurrent in Graphene. *Nature* **2007**, *446*, 56−59.
(35) Calado, V. E.; Goswami, S.; Nanda, G.; Diez, M.; Akhmerov, A. R.; Watanabe, K.; Taniguchi, T.; Klapwijk, T. M.; Vandersypen, L. M. K. Ballistic Josephson Junctions in Edge-Contacted Graphene. *Nat. Nanotechnology* **2015**, *10*, 761−764.
(36) Lee, G.-H.; Lee, H.-J. Proximity Coupling in Superconductor-Graphene Heterostructures. *Rep. Prog. Phys.* **2018**, *81*, 056502.
(37) Ben Shalom, M.; Zhu, M. J.; Fal'ko, V. I.; Mishchenko, A.; Kretinin, A. V.; Novoselov, K. S.; Woods, C.; Watanabe, K.; Taniguchi, T.; Geim, A. K.; Prance, J. R. Quantum Oscillations of the Critical Current and High-Field Superconducting Proximity in Ballistic Graphene. *Nat. Phys.* **2016**, *12*, 318−322.
(38) Amet, F.; Ke, C. T.; Borzenets, I. V.; Wang, J.; Watanabe, K.; Taniguchi, T.; Deacon, R. S.; Yamamoto, M.; Bomze, Y.; Tarucha, S.; Finkelstein, G. Supercurrent in the Quantum Hall Regime. *Science* **2016**, *352*, 966−969.
(39) Park, G.-H.; Kim, M.; Watanabe, K.; Taniguchi, T.; Lee, H.-J. Propagation of Superconducting Coherence *via* Chiral Quantum-Hall Edge Channels. *Sci. Rep.* **2017**, *7*, 10953.
(40) Lee, G.-H.; Huang, K.-F.; Efetov, D. K.; Wei, D. S.; Hart, S.; Taniguchi, T.; Watanabe, K.; Yacoby, A.; Kim, P. Inducing Superconducting Correlation in Quantum Hall Edge States. *Nat. Phys.* **2017**, *13*, 693−698.
(41) Önder, G.; Ronen, Y.; Lee, S. Y.; Shapourian, H.; Zauberman, J.; Lee, Y. H.; Watanabe, K.; Taniguchi, T.; Vishwanath, A.; Yacoby, A.; Kim, P. Induced Superconductivity in the Fractional Quantum Hall Edge. *ArXiv*, **2021**, arXiv:2009.07836.
(42) Stern, A.; Lindner, N. H. Topological Quantum Computation—From Basic Concepts to First Experiments. *Science* **2013**, *339*, 1179−1184.
(43) Carrega, M.; Chirolli, L.; Heun, S.; Sorba, L. Anyons in Quantum Hall Interferometry. *Nat. Rev. Phys.* **2021**, *3*, 698−711.
(44) Chen, W.; et al. High-Quality *in situ* Fabricated Nb Josephson Junctions with Black Phosphorus Barriers. *Supercond. Sci. Technol.* **2019**, *32*, 115005.
(45) Xu, Z.; et al. Vertical Josephson Field-Effect Transistors Based on Black Phosphorus. *Appl. Phys. Lett.* **2021**, *119*, 072601.
(46) Ramezani, M.; Sampaio, I. C.; Watanabe, K.; Taniguchi, T.; Schönenberger, C.; Baumgartner, A. Superconducting Contacts to a Monolayer Semiconductor. *Nano Lett.* **2021**, *21*, 5614−5619.
(47) Keyes, R. W. The Electrical Properties of Black Phosphorus. *Phys. Rev.* **1953**, *92*, 580−584.
(48) Warschauer, D. Electrical and Optical Properties of Crystalline Black Phosphorus. *J. Appl. Phys.* **1963**, *34*, 1853−1860.
(49) Morita, A. Semiconducting Black Phosphorus. *Appl. Phys. A: Mater. Sci. Process.* **1986**, *39*, 227−242.
(50) Telesio, F.; Hemsworth, N.; Dickerson, W.; Petrescu, M.; Tayari, V.; Yu, O.; Graf, D.; Serrano-Ruiz, M.; Caporali, M.; Peruzzini, M.; Carrega, M.; Szkopek, T.; Heun, S.; Gervais, G. Nonclassical

https://doi.org/10.1021/acsnano.1c09315
ACS Nano 2022, 16, 3538−3545

Longitudinal Magnetoresistance in Anisotropic Black Phosphorus. *Phys. Status Solidi RRL* **2020**, *14*, 1900347.
(51) Linder, J.; Yokoyama, T. Anisotropic Andreev Reflection and Josephson Effect in Ballistic Phosphorene. *Phys. Rev. B* **2017**, *95*, 144515.
(52) Alidoust, M.; Willatzen, M.; Jauho, A.-P. Fraunhofer Response and Supercurrent Spin Switching in Black Phosphorus with Strain and Disorder. *Phys. Rev. B* **2018**, *98*, 184505.
(53) Alidoust, M.; Willatzen, M.; Jauho, A.-P. Control of Superconducting Pairing Symmetries in Monolayer Black Phosphorus. *Phys. Rev. B* **2019**, *99*, 125417.
(54) Grosso, G.; Parravicini, G. P. *Solid State Physics*, 2nd Ed.; Academic Press, Elsevier, 2014.
(55) Ambegaokar, V.; Halperin, B. I. Voltage Due to Thermal Noise in the dc Josephson Effect. *Phys. Rev. Lett.* **1969**, *22*, 1364−1366.
(56) Gross, R.; Marx, A. *Applied Superconductivity: Josephson Effect and Superconducting Electronics*; Walther-Meißner-Institut: Garching, 2005.
(57) Belogolovskii, M.; Zhitlukhina, E.; Lacquaniti, V.; De Leo, N.; Fretto, M.; Sosso, A. Intrinsically Shunted Josephson Junctions for Electronics Applications. *Low Temperature Physics* **2017**, *43*, 756−765.
(58) Zhukovskii, V. C.; Pozdnyakova, O. D.; Krevchik, V. D.; Semenov, M. B.; Shorokhov, A. V. The Influence of the McCumber Parameter on Parametric Amplification of High-Frequency Radiation by Josephson Junctions. *Mosc. Univ. Phys. B+* **2018**, *73*, 211−215.
(59) Telesio, F.; le Gal, G.; Serrano-Ruiz, M.; Prescimone, F.; Toffanin, S.; Peruzzini, M.; Heun, S. Ohmic Contact Engineering in Few−Layer Black Phosphorus: Approaching the Quantum Limit. *Nanotechnology* **2020**, *31*, 334002.
(60) Ando, T.; Fowler, A. B.; Stern, F. Electronic Properties of Two-Dimensional Systems. *Rev. Mod. Phys.* **1982**, *54*, 437−672.
(61) Chrestin, A.; Matsuyama, T.; Merkt, U. Evidence for a Proximity-Induced Energy Gap in Nb/InAs/Nb Junctions. *Phys. Rev. B* **1997**, *55*, 8457−8465.
(62) Qiao, J.; Kong, X.; Hu, Z.-X.; Yang, F.; Ji, W. High-Mobility Transport Anisotropy and Linear Dichroism in Few-Layer Black Phosphorus. *Nat. Commun.* **2014**, *5*, 4475.
(63) Mur, L. C.; Harmans, C. J. P. M.; Mooij, J. E.; Carlin, J. F.; Rudra, A.; Ilegems, M. Experimental Indication for Supercurrents Carried by Opened Transport Channels. *Phys. Rev. B* **1996**, *54*, R2327−R2330.
(64) Courtois, H.; Gandit, P.; Mailly, D.; Pannetier, B. Long-Range Coherence in a Mesoscopic Metal near a Superconducting Interface. *Phys. Rev. Lett.* **1996**, *76*, 130−133.
(65) Pannetier, B.; Courtois, H. Andreev Reflection and Proximity Effect. *J. Low Temp. Phys.* **2000**, *118*, 599−615.
(66) Dubos, P.; Courtois, H.; Pannetier, B.; Wilhelm, F. K.; Zaikin, A. D.; Schön, G. Josephson Critical Current in a Long Mesoscopic S-N-S Junction. *Phys. Rev. B* **2001**, *63*, 064502.
(67) Kuprianov, M. Y.; Lukichev, V. F. Influence of Boundary Transparency on the Critical Current of "dirty" *SS′S* Structures. *Sov. Phys. JETP* **1988**, *67*, 1163−1168.
(68) Heikkilä, T. T.; Särkkä, J.; Wilhelm, F. K. Supercurrent-Carrying Density of States in Diffusive Mesoscopic Josephson Weak Links. *Phys. Rev. B* **2002**, *66*, 184513.
(69) Halperin, B. I.; Refael, G.; Demler, E. Resistance in Superconductors. *International Journal of Modern Physics B* **2010**, *24*, 4039−4080.
(70) Courtois, H.; Gandit, P.; Pannetier, B. Proximity-Induced Superconductivity in a Narrow Metallic Wire. *Phys. Rev. B* **1995**, *52*, 1162−1166.
(71) Wilhelm, F. K.; Zaikin, A. D.; Schön, G. Supercurrent in a Mesoscopic Proximity Wire. *J. Low Temp. Phys.* **1997**, *106*, 305−310.
(72) de Vries, F. K.; Sol, M. L.; Gazibegovic, S.; op het Veld, R. L. M.; Balk, S. C.; Car, D.; Bakkers, E. P. A. M.; Kouwenhoven, L. P.; Shen, J. Crossed Andreev Reflection in InSb Flake Josephson Junctions. *Phys. Rev. Research* **2019**, *1*, 032031.
(73) Baumgartner, C.; Fuchs, L.; Frész, L.; Reinhardt, S.; Gronin, S.; Gardner, G. C.; Manfra, M. J.; Paradiso, N.; Strunk, C. Josephson Inductance As a Probe for Highly Ballistic Semiconductor-Superconductor Weak Links. *Phys. Rev. Lett.* **2021**, *126*, 037001.
(74) Chiodi, F.; Ferrier, M.; Guéron, S.; Cuevas, J. C.; Montambaux, G.; Fortuna, F.; Kasumov, A.; Bouchiat, H. Geometry-Related Magnetic Interference Patterns in Long *SNS* Josephson Junctions. *Phys. Rev. B* **2012**, *86*, 064510.
(75) Maxfield, B. W.; McLean, W. L. Superconducting Penetration Depth of Niobium. *Phys. Rev.* **1965**, *139*, A1515−A1522.
(76) Suominen, H. J.; Danon, J.; Kjaergaard, M.; Flensberg, K.; Shabani, J.; Palmstrøm, C. J.; Nichele, F.; Marcus, C. M. Anomalous Fraunhofer Interference in Epitaxial Superconductor-Semiconductor Josephson Junctions. *Phys. Rev. B* **2017**, *95*, 035307.
(77) Monteiro, A. M. R. V. L.; Groenendijk, D. J.; Manca, N.; Mulazimoglu, E.; Goswami, S.; Blanter, Y.; Vandersypen, L. M. K.; Caviglia, A. D. Side Gate Tunable Josephson Junctions at the $LaAlO_3$/$SrTiO_3$ Interface. *Nano Lett.* **2017**, *17*, 715−720.
(78) Viti, L.; Hu, J.; Coquillat, D.; Knap, W.; Tredicucci, A.; Politano, A.; Vitiello, M. S. Black Phosphorus Terahertz Photodetectors. *Adv. Mater.* **2015**, *27*, 5567−5572.
(79) Guo, Q.; Pospischil, A.; Bhuiyan, M.; Jiang, H.; Tian, H.; Farmer, D.; Deng, B.; Li, C.; Han, S.-J.; Wang, H.; Xia, Q.; Ma, T.-P.; Mueller, T.; Xia, F. Black Phosphorus Mid-Infrared Photodetectors with High Gain. *Nano Lett.* **2016**, *16*, 4648−4655.
(80) Giordano, M. C.; Viti, L.; Mitrofanov, O.; Vitiello, M. S. Phase-Sensitive Terahertz Imaging Using Room-Temperature Near-Field Nanodetectors. *Optica* **2018**, *5*, 651−657.
(81) Walsh, E. D.; Efetov, D. K.; Lee, G.-H.; Heuck, M.; Crossno, J.; Ohki, T. A.; Kim, P.; Englund, D.; Fong, K. C. Graphene-Based Josephson-Junction Single-Photon Detector. *Phys. Rev. Applied* **2017**, *8*, 024022.
(82) Nilges, T.; Kersting, M.; Pfeifer, T. A Fast Low-Pressure Transport Route to Large Black Phosphorus Single Crystals. *J. Solid State Chem.* **2008**, *181*, 1707−1711.
(83) Cappelli, G. Quantum Transport in Planar Niobium/Black-Phosphorus/Niobium Junctions. M.Sc. thesis, University of Pisa, 2020.
(84) Usadel, K. D. Generalized Diffusion Equation for Superconducting Alloys. *Phys. Rev. Lett.* **1970**, *25*, 507−509.

https://doi.org/10.1021/acsnano.1c09315
ACS Nano 2022, 16, 3538−3545